Physical characteristics of scattered radiation in diagnostic radiology: Monte Carlo simulation studies

HeangPing Chan and Kunio Doi

Physical characteristics of scattered radiation in diagnostic radiology: Monte Carlo simulation studies

Heang-Ping Chan and Kunio Doi

Kurt Rossmann Laboratories for Radiologic Image Research, Department of Radiology, The University of Chicago, Chicago, Illinois 60637

We applied Monte Carlo methods for the simulation of x-ray scattering in water phantoms. The phantom thickness was varied from 5 to 20 cm, and the monoenergetic incident x rays were varied from 15 to 100 keV. Eight screen pairs and a total absorption system were used as x-ray receptors. We determined the angular, spectral, and spatial distributions of the scattered radiation and the scatter fractions recorded in the image plane. The dependence of these properties on the incident x-ray energy, the phantom thickness, and the energy response of the recording system was examined. The results of this study provide useful information for the development of antiscatter techniques and for the evaluation of radiographic procedures.

I. INTRODUCTION

In diagnostic radiology, image contrast is degraded significantly by scattered radiation. It is therefore important to understand the physical characteristics of scattered radiation so that effective antiscatter techniques can be developed for the improvement of diagnostic accuracy. Antiscatter techniques are based primarily on differences in the angular distributions and, to a lesser extent, in the spectral distributions of primary and scattered radiation.

Very limited experimental data have been published regarding the angular and spectral distributions of scattered radiation emerging from a tissue-equivalent phantom irradiated with x rays in the diagnostic energy range. Past measurements[1-3] were confined to a few specific imaging conditions. The technical difficulties involved in experimental studies are probably responsible for the limited investigations performed.

Theoretical investigations of the properties of scattered radiation have also been attempted. Monte Carlo calculation has proven to be by far the most successful method for the simulation of the stochastic process of x-ray diffusion in a scattering medium.[2,4-14] In the present study, we applied the Monte Carlo methods to the systematic analysis of the angular, spectral, and spatial distributions of scattered radiation, and of the scatter fraction recorded by the x-ray receptor. The dependence of these properties on the incident x-ray energy, phantom thickness, and the energy response of the recording system was examined. This information provides a basis for the development of antiscatter techniques and for the evaluation of radiographic procedures.

II. INPUT PARAMETERS

Our Monte Carlo methods, the input data used, and their validity for the simulation of photon scattering have been described in detail previously.[9,12] In this study, the incident radiation was assumed to be a pencil ray impinging normally on the surface of a plane, parallel, homogeneous water phantom. The phantom was infinite in area, and its thickness was varied from 5 to 20 cm in 5-cm increments. These thicknesses simulate the tissue thickness of different body parts. The attenuation coefficients for the photoelectric effect, co-

herent scattering, and incoherent scattering processes in water were calculated from the elemental cross-section data tabulated by Storm and Israel.[15]

A pair of screens placed behind the phantom and parallel to its posterior surface served as the radiation detector. The methods used for the calculation of the radiographic response of screen–film systems have also been discussed elsewhere.[16] We included eight screens, namely, Detail ($CaWO_4$), Par Speed ($CaWO_4$), Hi-Plus ($CaWO_4$), Lanex Regular (Gd_2O_2S), X-Omatic Regular ($BaSrSO_4$), Quanta II ($BaFCl$), Quanta III ($LaOBr$), and BG Mid Speed (Gd_2O_2S/Y_2O_2S), as well as a total-absorption system, which was assumed to absorb all incident photons. The x-ray absorption properties of these screens were examined in earlier studies.[16]

We employed monoenergetic x rays of energies from 15 to 100 keV in 5-keV increments as the incident beam. Thus, we were able to investigate the energy-dependent properties of scattered radiation.

III. RESULTS

A. Angular distribution of scattered radiation

1. Angular distribution of singly scattered photons

In Fig. 1(a) the differential cross section of single coherent scattering in water,

$$f_{coh}(\theta) = \frac{1}{\pi r_0^2} \frac{d\sigma_{coh}}{d\theta} = (1 + \cos^2 \theta) \sin \theta \, F_m^2(v^2), \quad (1)$$

is plotted as a function of the scattering angle θ. $F_m(v^2)$ is the form factor of water molecules, and $v = E \sin(\theta/2)/hc$, where $2hv$ is the momentum transfer in the photon–electron collision, E is the photon energy, h is the Planck's constant, and c is the speed of light. r_0 is the classical electron radius. The form factor of water was calculated[12] from the atomic form factors[17,18] by assuming that the interatomic and intermolecular interference effects of coherently scattered x rays were negligible. Inclusion of these effects may affect the angular distributions at small scattering angles. We will discuss in greater detail the significance of these effects on the properties of scattered radiation in Sec. IV.

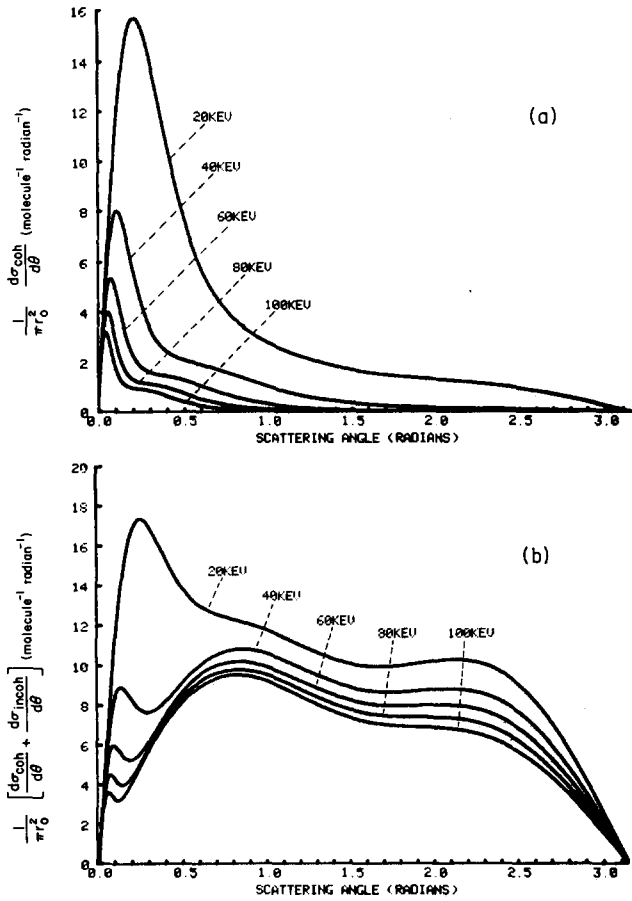Figure 1(b) shows the sum of differential cross sections of

FIG. 1. Angular distributions of singly scattered photons in water: (a) single coherent scattering and (b) single coherent and incoherent scattering, for incident photons energies between 20 and 100 keV.

EXIT ANGLE OF SCATTERED PHOTONS (DEGREES)

FIG. 2. Angular distributions of scattered photons, in terms of relative number of scattered photons per unit exit angle, emerging from water phantoms of thicknesses (a) 5, (b)10, (c) 15, and (d) 20 cm, for monoenergetic incident x rays of energies between 20 and 100 keV.

coherent and incoherent scattering in water, given by

$$f(\theta) = \frac{1}{\pi r_0^2}\left[\frac{d\sigma_{coh}}{d\theta} + \frac{d\sigma_{incoh}}{d\theta}\right]$$

$$= \frac{2\sin\theta}{r_0^2}\left[\frac{d\sigma_{Thomson}}{d\Omega}F_m^2(v^2) + \frac{d\sigma^{KN}}{d\Omega}S_m(v)\right], \quad (2)$$

where $d\sigma_{Thomson}/d\Omega$ and $d\sigma^{KN}/d\Omega$ are the Thomson and Klein–Nishina differential cross sections, respectively. $S_m(v)$ is the incoherent-scattering function for water molecules[12] calculated from the atomic incoherent-scattering functions.[19,20] The differential cross section $f(\theta)$ can be regarded as the angular distribution of scattered photons when the x-ray beam is incident on an infinitesimally thin water phantom so that a given photon can undergo at most one interaction.

2. Relative number of scattered photons per unit exit angle

For the geometry studied, the angular distribution of the scattered photons is assumed to be rotationally symmetric about the incident beam. The angular distribution of scattered photons exiting the phantom can be expressed as the relative number of scattered photons per unit exit angle as a function of the exit angle, which is defined as the polar angle θ between the direction of the primary beam and that of a scattered photon. In our calculations, the scattered photons were collected in 5° intervals of the exit angle, and the maxi-
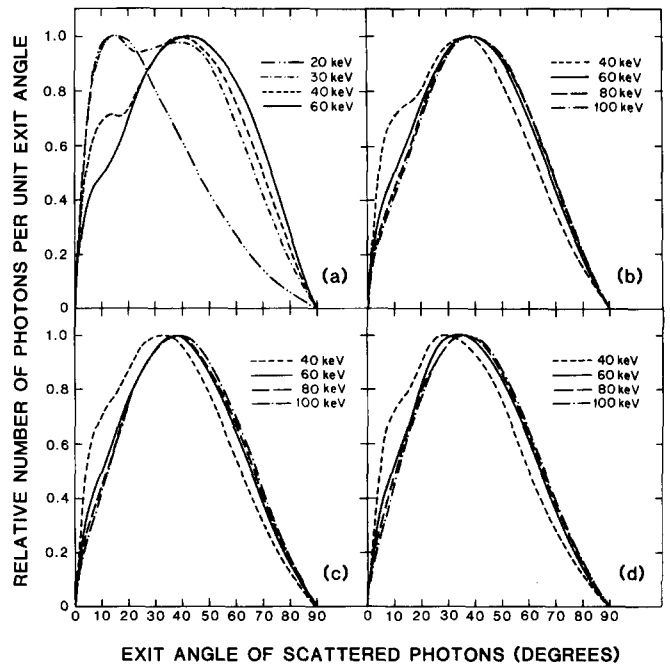
mum of each distribution was normalized to unity. The resulting angular distributions of scattered radiation are shown in Figs. 2(a)–2(d). Comparisons of the distributions for the four phantoms at incident energies of 50 and 90 keV are shown in Figs. 3(a)–3(b).

The angular distributions are approximately bell-shaped curves with a small-angle scatter component in the region below 15°. This component decreases in magnitude and shifts to smaller exit angles as the incident energy increases. With the 5-cm phantom, the angular distribution for a 20-keV incident beam is actually dominated by the small-angle component. For a given incident energy, the thicker the phantom, the lower the probability that a scattered photon will emerge from the phantom in the range of the small-angle component. Furthermore, the most probable exit angle of the scattered photons decreases with increasing phantom thickness. Some characteristics of these angular distributions can be explained by reference to the distribution of singly scattered photons shown in Fig. 1.

The general features of the angular distributions for single scattering are compatible with the characteristics of the small-angle component observed in the angular distributions for a phantom of finite thickness. Photons that have undergone a single coherent scattering event are more likely to escape from the phantom than are the incoherently scattered photons, since they carry the original photon energy and since the smaller scattering angle results in a shorter path length which the photon has to travel in the phantom. The coherently scattered photons can thus significantly affect the angular distribution of the scattered radiation when the probability of multiple scattering is low. This influence decreases when the incident energy increases, due to the rapid reduction in the cross section of coherent scattering.

FIG. 4. Dependence of the mean exit angle of scattered photons on incident x-ray energy.
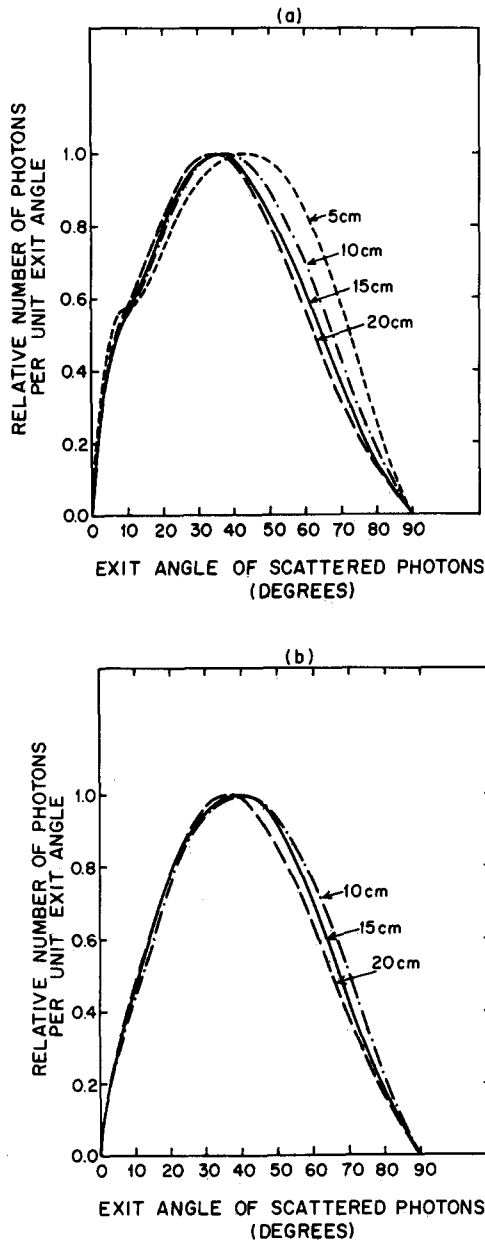

FIG. 3. Angular distributions of scattered photons, in terms of relative number of scattered photons per unit exit angle, emerging from water phantoms of thicknesses between 5 and 20 cm, for monoenergetic incident x rays of energies (a) 50 and (b) 90 keV.

3. Dependence of mean exit angle of scattered radiation on incident energy

The mean exit angle of the transmitted scattered photons, averaged over scattered photons of all energies, was determined as a function of incident photon energy for the four water phantoms. The results are shown in Fig. 4. For a given phantom, the mean exit angle increases gradually as the energy increases. This can be attributed to the decreasing probability of coherent scattering in combination with the increasing probability of multiple scattering, which tends to yield a more isotropic angular distribution. For a given energy, the mean exit angle is smaller for thicker phantoms, probably because the escaping photons have to travel long distances in a thick phantom, so that those with a smaller
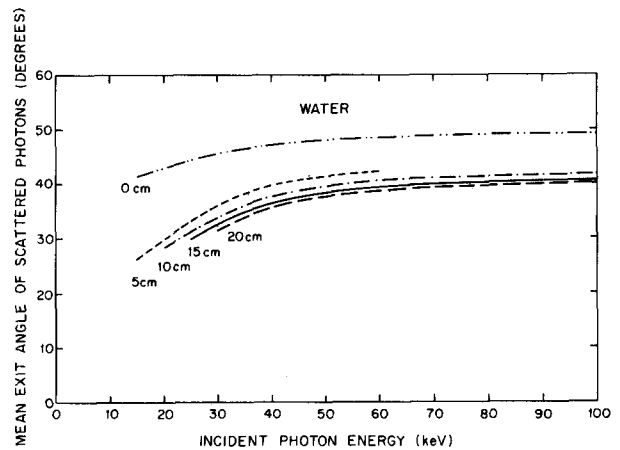
exit angle, and hence on the average a shorter path length, have a higher probability of escaping from the phantom. This "filtration effect" overcomes the effect of the higher probability of multiple scattering in a thick phantom and results in a more forward directed angular distribution. For phantoms with thicknesses between 10 and 20 cm, the mean exit angle is about 40° for incident energies above 60 keV.

The mean exit angle of scattered photons emerging from a water phantom of infinitesimal thickness was calculated analytically from the differential cross section in Eq. (2). The mean exit angle was found to increase gradually from about 41° to 49° as the incident x-ray energy increases from 15 to 100 keV.

4. Relative number of scattered photons per unit solid angle

The angular distribution expressed in terms of the relative number of scattered photons per unit solid angle is plotted as a function of exit angle in Figs. 5(a)–5(d). The number of scattered photons is normalized to 100 incident photons. In spite of the small number of scattered photons that emerge with small exit angles, a sharp rise is observed around the central ray because of the small solid angle in this region. As is to be expected, the thicker the phantom or the lower the incident energy, the smaller the number of scattered photons penetrating the phantom at all exit angles. The angular distributions expressed in terms of the number of scattered photons per unit solid angle correspond to those which would be measured with a collimated detector, subtending a unit solid angle, viewing at the exit surface of the phantom.

Most of the antiscatter devices presently in use are designed as one-dimensional parallel arrays of lead strips, such as linear grids and a scanning multiple-slit assembly.[21,22] For evaluation of the effectiveness of these devices, the pertinent angular distribution is the one-dimensional distribution as a function of the angle in the direction perpendicular to the lead strips. One can derive these distributions from the two-dimensional distributions by transforming the coordinate system and integrating numerically along one direction. The detailed formulation of this procedure is described elsewhere.[9]
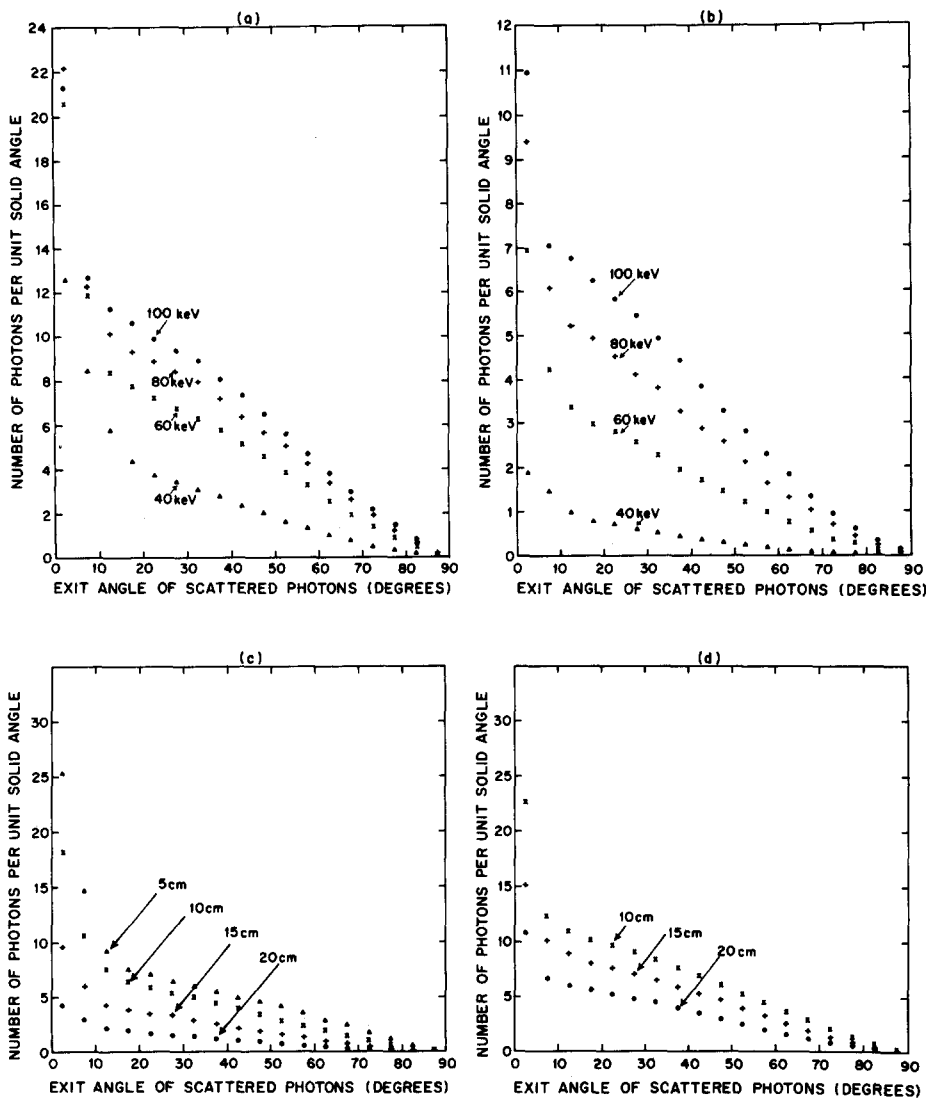
FIG. 5. Angular distributions of scattered photons, in terms of relative number of scattered photons per unit solid angle (sr^{-1}), emerging from water phantoms of thicknesses (a) 10 and (b) 20 cm, for incident x rays of energies between 40 and 100 keV; and from water phantoms of thicknesses between 5 and 20 cm, for incident x rays of energies (c) 50 and (d) 90 keV. The number of scattered photons is normalized to 100 incident photons.

The one-dimensional angular distributions derived from the distributions shown in Figs. 5(a)–5(d) are plotted in Figs. 6(a)–6(d). Similar to the two-dimensional distributions, the relative number of scattered photons is larger for higher incident energies and for thinner phantoms. Both effects are caused by the larger number of scattered photons which can penetrate the phantom.

These derived one-dimensional angular distributions can be used to estimate the effectiveness of an antiscatter device behind the phantom when there is no interspace material in the radiopaque array of high-Z material. However, for an antiscatter device with interspace material which can absorb scattered photons, the capability of the device to eliminate the scattered photons depends on the energy as well as the path length of the photons in the interspace material. In this case, the angular distribution to be used for the evaluation of absorption of scattered photons by the device needs to be the more basic two-dimensional one. Furthermore, if the interaction of x rays in the antiscatter device can contribute significantly to the scattered radiation behind the device, it will be necessary to apply Monte Carlo calculations to simulate photon histories in the device material[12] in order to determine the effectiveness of the device.

B. Spectral content of scattered radiation

1. Dependence of spectral distribution of scattered radiation on exit angle

By sorting the scattered photons into different angular ranges and, in each angular range, into different energy windows, we obtained the spectral content of the scattered radiation in each angular range. A 10° angular interval and a 2-keV energy window were employed for determining the spectra of scattered radiation illustrated in Figs. 7(a)–7(d) and 8(a)–8(d).

The spectral distributions show that, at small exit angles, a large fraction of the transmitted scattered photons has approximately the same energy as does the incident energy. These photons include those which have undergone coherent scattering or small-angle Compton scattering. From the photon histories, we found that the fraction of coherently scattered photons increases to a maximum with increasing energy and then decreases at higher energies; this fraction also decreases rapidly with increasing exit angle, since the probability of large-angle coherent scattering is small. The apparent increase in the number of photons (see Figs. 7 and 8) in the highest energy interval of the spectra in the 30° to 40°
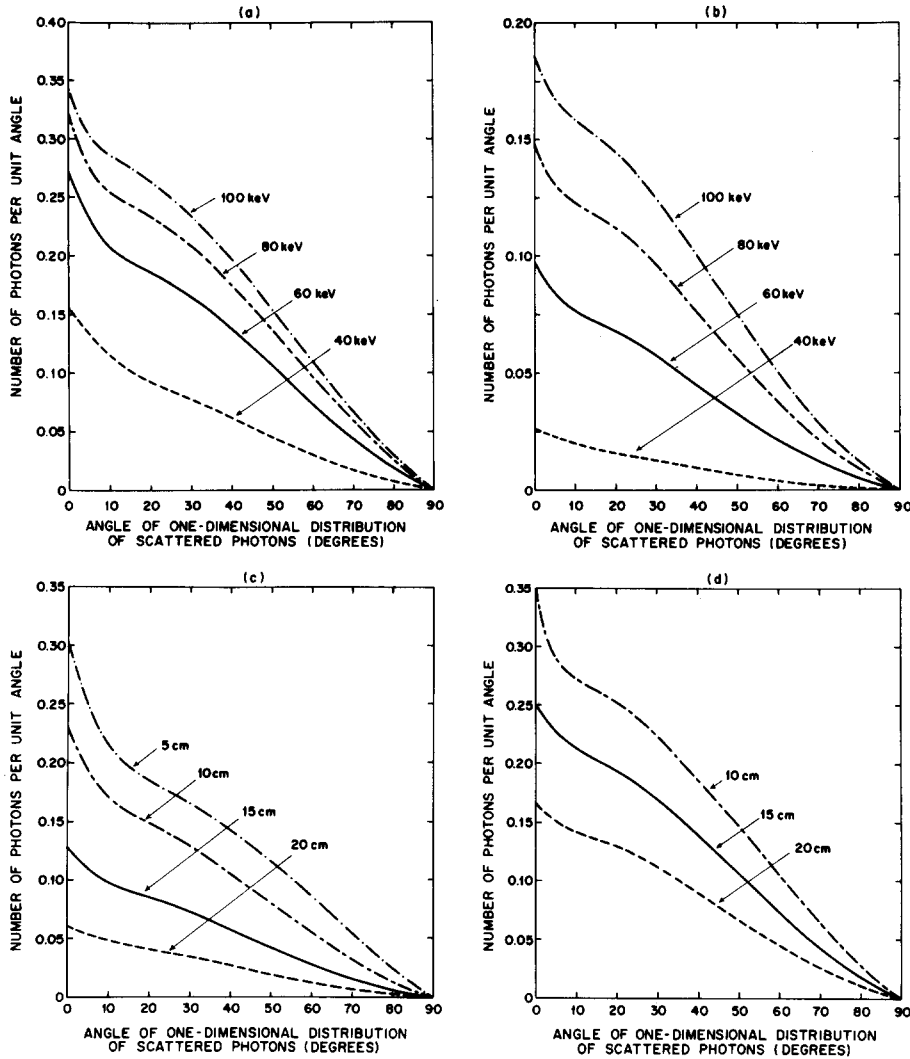
FIG. 6. One-dimensional angular distributions, in terms of relative number of scattered photons per unit angle (radian^{-1}), emerging from water phantoms of thicknesses (a) 10 and (b) 20 cm, for incident x rays of energies between 40 and 100 keV; and from water phantoms of thicknesses between 5 and 20 cm, for incident x rays of energies (c) 50 and (d) 90 keV. The number of scattered photons is normalized to 100 incident photons.

FIG. 7. Spectral distributions of scattered photons emerging from a 10-cm-thick phantom in exit angle ranges of 0°–10°, 30°– 40°, and 60°–70°, for incident x rays of energies (a) 40, (b) 60, (c) 80, and (d) 100 keV. The number of scattered photons is normalized to 100 incident photons.

(a)

(b)

(c)

(d)

30°-40°

0°-10°

60°-70°

PHOTON ENERGY (KEV)
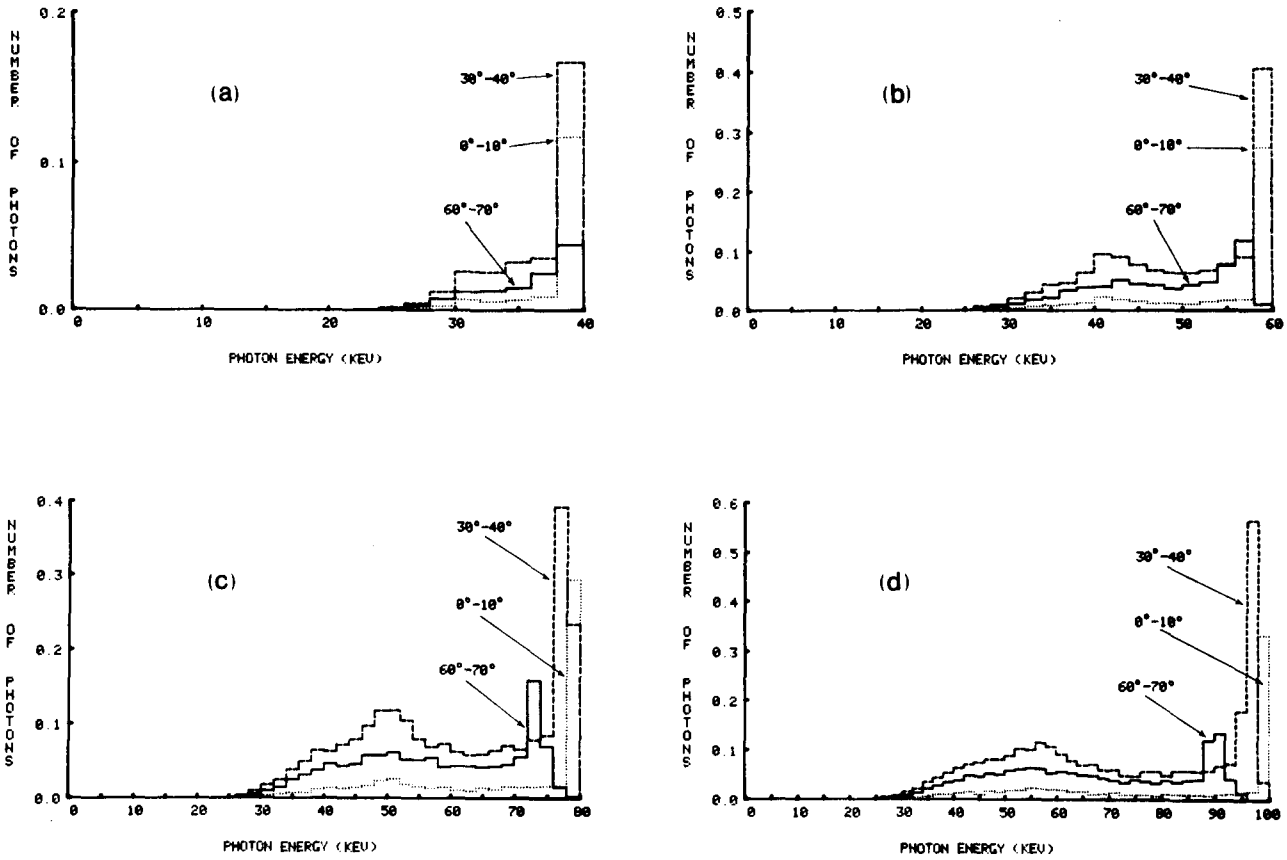
NUMBER OF PHOTONS

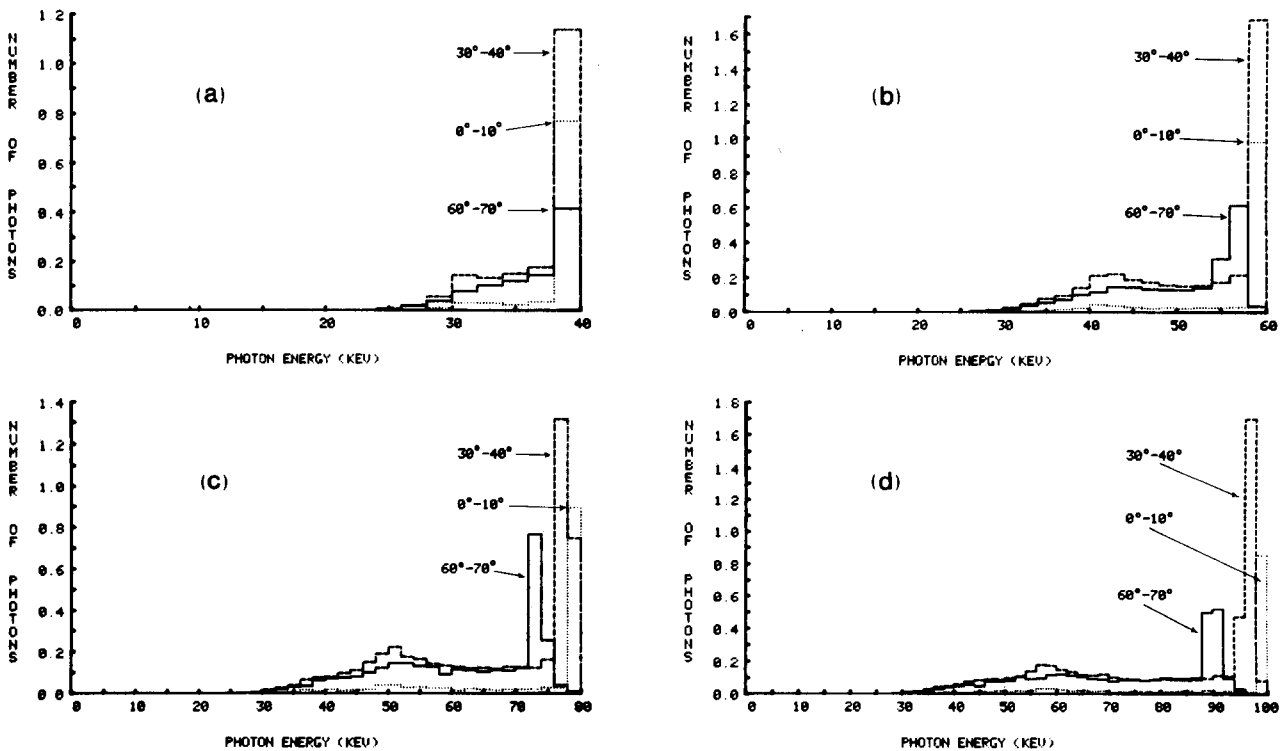FIG. 8. Spectral distributions of scattered photons emerging from a 20-cm-thick phantom in exit angle ranges of 0°-10°, 30° - 40°, and 60°-70°, for incident x rays of energies (a) 40, (b) 60, (c) 80, and (d) 100 keV. The number of scattered photons is normalized to 100 incident photons.

(a)

(b)

100 keV

80 keV

60 keV

40 keV

100 keV

10 cm
15 cm
20 cm

50 keV

5 cm
10 cm
15 cm
20 cm

MEAN ENERGY OF SCATTERED PHOTONS (keV)

EXIT ANGLE OF SCATTERED PHOTONS
(DEGREES)

FIG. 9. Dependence of mean energy on exit angle of scattered photons emerging (a) from a 20-cm-thick water phantom, for incident x rays between 40 and 100 keV; and (b) from water phantoms of thicknesses between 5 and 20 cm, for incident x rays of energies 50 and 100 keV.

FIG. 10. Spectral distributions of scattered photons for incident x rays of energies (a) 40 and (b) 60 keV. The thicknesses of the water phantoms are 10 and 20 cm. The number of scattered photons is normalized to 100 incident photons.

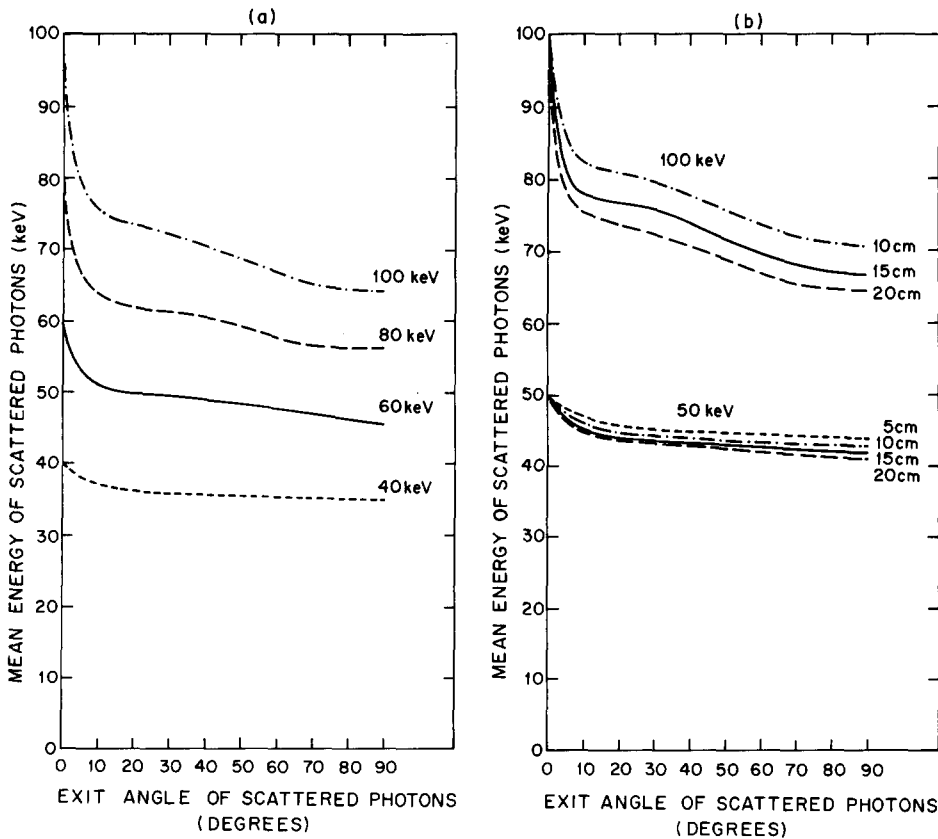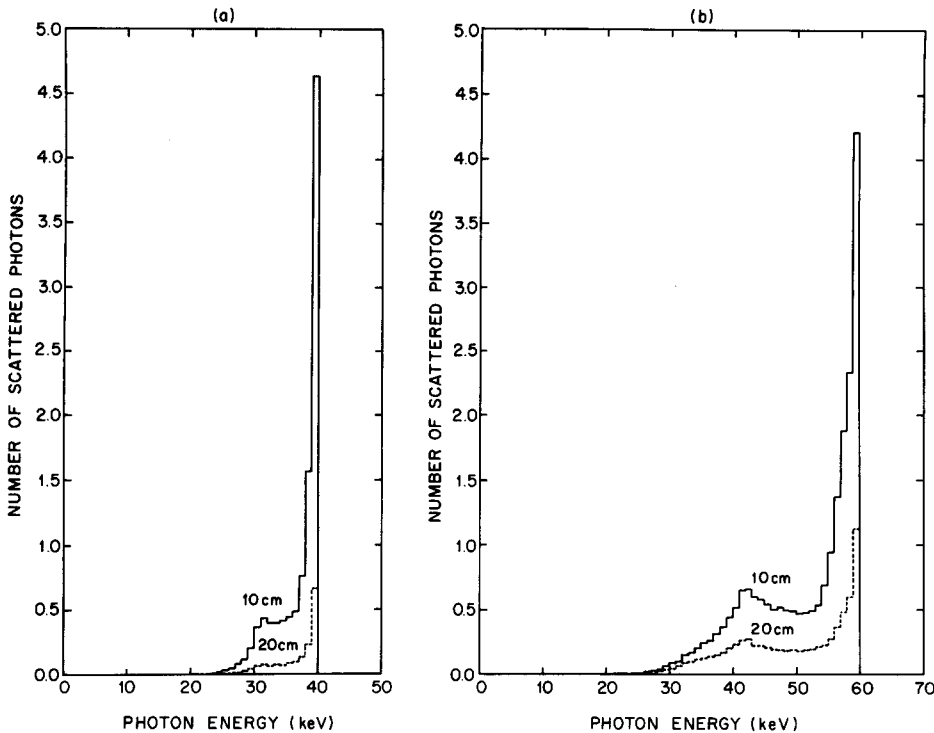range, as compared to that of the spectra in the 0° to 10° range, for the 40- and 60-keV incident beams is due to the Compton-scattered photons which lose less than 2 keV of their energy.

For a given phantom, the fraction of low-energy scattered photons increases as the incident energy increases, due to the increase in the probability of multiple scattering and the decrease in the absorption cross section. For a given incident energy, larger exit angles correspond to softer scattered radiation. Furthermore, when the phantom thickness increases, the total number of emerging scattered photons decreases and the spectrum in each angular range shifts to the lower energy region, simply because fewer photons can escape from a thicker phantom and because the probability of multiple scattering increases.

2. Dependence of the mean energy of scattered radiation on exit angle

The mean energies of the scattered x-ray spectra emerging from the phantom in different ranges of exit angles were calculated and are shown in Figs. 9(a)–9(b). A 5° increment of exit angle was used in the calculations. For incident energies below 40 keV, the mean energy decreases by less than 5 keV as the exit angle varies from 0° to 90°, whereas for a 100-keV beam, the variation can be as large as 35 keV. The drop in the mean energy occurs primarily within exit angles between 0° and 10°. The shapes of the curves for different phantom thicknesses are similar. As can be expected, for the same exit angle, the thicker the phantom, the lower the mean energy.

3. Spectral distribution of scattered radiation

The spectral distribution of all transmitted scattered photons is the sum of the spectra at all exit angles. Figures 10(a)–10(b) and 11(a)–11(b) show the spectra of transmitted scat-

tered photons. These spectra were determined for energy intervals of 1 keV and normalized to 100 incident photons. It can be seen that, when the phantom thickness increases, the fraction of high-energy scattered photons decreases relative
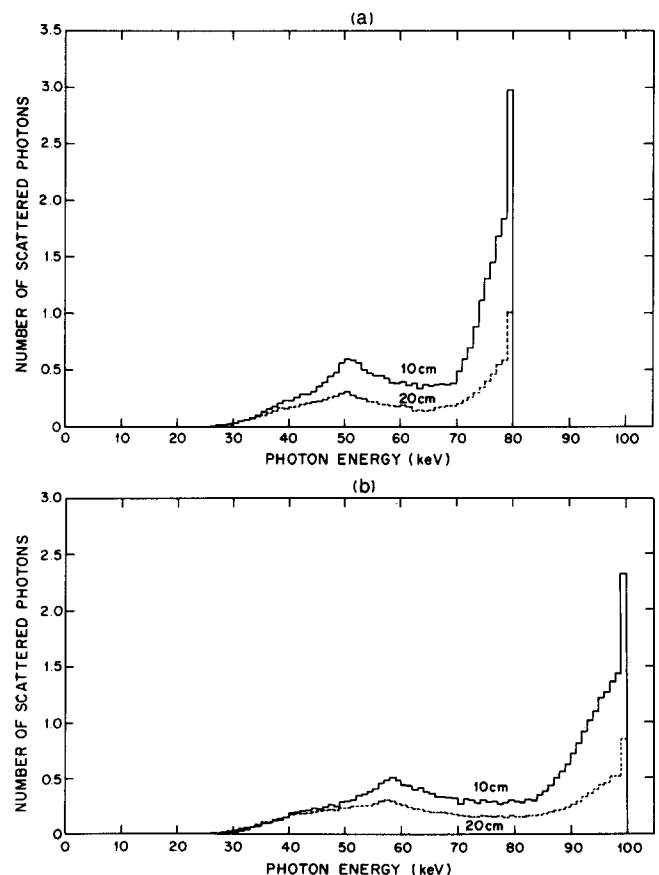

FIG. 11. Spectral distributions of scattered photons for incident x rays of energies (a) 80 and (b) 100 keV. The thicknesses of the water phantoms are 10 and 20 cm. The number of scattered photons is normalized to 100 incident photons.
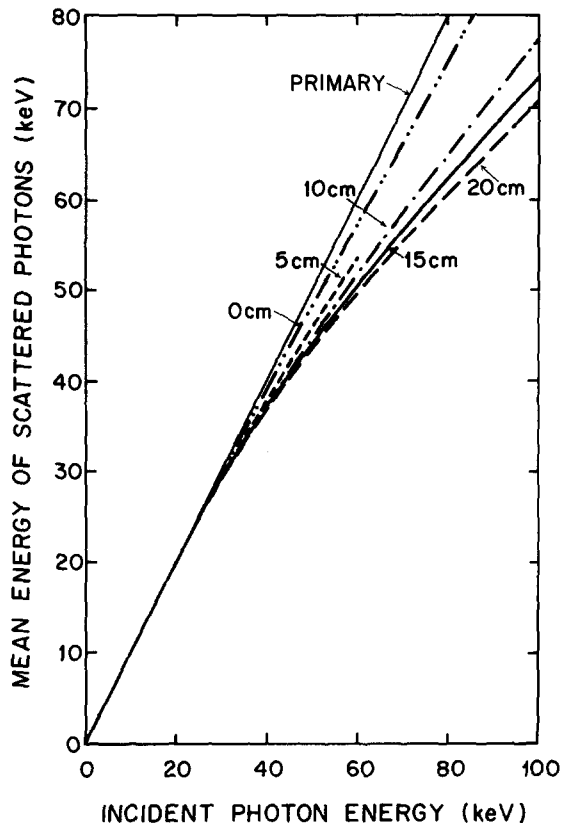
FIG. 12. Mean energy of scattered photons emerging from water phantoms of thicknesses up to 20 cm, as a function of incident x-ray energy.
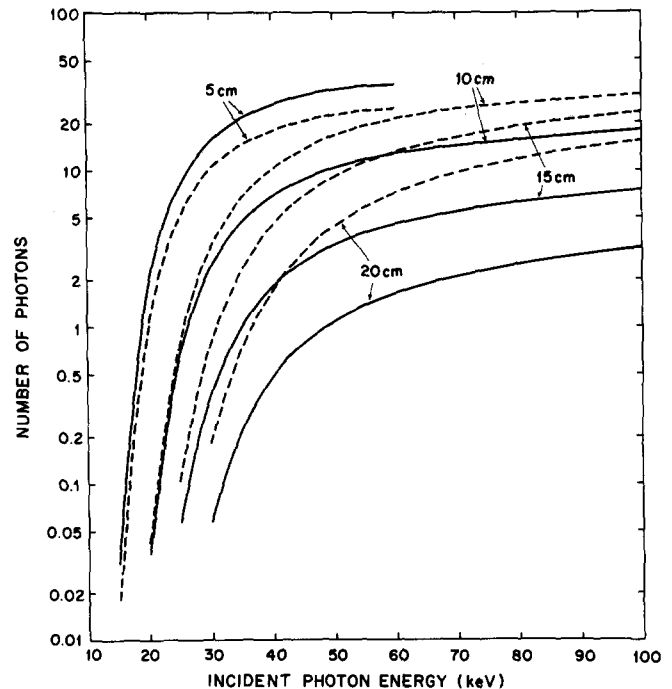

FIG. 13. Dependence of numbers of transmitted primary photons (—) and scattered photons (---) on incident x-ray energy for water phantoms of thicknesses between 5 and 20 cm. The number of scattered photons is normalized to 100 incident photons.

to that of the low-energy photons because of the higher probability of multiple scattering in a thicker phantom. The energies of the photons scattered at 90° in a Compton event for 40-, 60-, 80-, and 100-keV incident photons are 37.1, 53.7, 69.2, and 83.6 keV, respectively. The transmitted scattered photons which have energies below these values have lost their energy through multiple scattering. The portions of the spectra above these energies include both singly and multiply scattered photons. It should be noted that, for incident energies above 40 keV, transmitted scattered photons with energies below 30 keV constitute only a negligible fraction of the scattered radiation.

4. Mean energy of scattered radiation

The mean energy of the transmitted scattered photons is plotted in Fig. 12 as a function of incident photon energy. The straight solid line represents the energy of the transmitted monoenergetic primary x rays. The mean energy of the scattered radiation is always lower than the incident energy because a part of the photon energy has been transferred to the scattering medium. The 0-cm curve indicates the mean energy of scattered photons transmitted through a water phantom of infinitesimal thickness. The results were calculated analytically from the angular distribution of singly scattered photons [Eq. (2)] in the forward direction.

As was observed previously from the spectral distributions, the thicker the phantom, the softer the scattered radiation. For incident energies below about 30 keV, the mean energy is approximately the same as the primary radiation

for all of the phantom thicknesses. The difference in the mean energies for the different phantom thicknesses increases with increasing energy of the incident photons.

5. Numbers of transmitted primary and scattered photons

The numbers of transmitted primary photons and scattered photons for the four phantoms are plotted in Fig. 13. The solid curves for the primary photons agree with those which can be calculated analytically by using the exponential survival probability and the total attenuation coefficients. For the 5-cm phantom, more primary photons than scattered photons are transmitted. However, as the phantom thickness increases, the scattered radiation becomes the dominant component. The ratio of the number of scattered photons to the number of primary photons increases with increasing incident energy; for each phantom thickness, it approaches an almost constant value above 60 keV. The ratios are approximately 0.7, 1.7, 3.1, and 4.8 at high energies for the 5-, 10-, 15-, and 20-cm phantoms, respectively. The total energies of the scattered radiation and primary radiation penetrating through the phantom can be estimated from the total numbers and the mean energies of the photons, which were shown in Fig. 12.

C. Spatial distribution of scattered radiation in the image plane

The scattered radiation emerging from the phantom toward the image plane may be detected by a recording system. For a pencil beam incident normally on a plane, parallel, homogeneous phantom and a uniform recording system such as a screen–film system, the recorded spatial distribu-
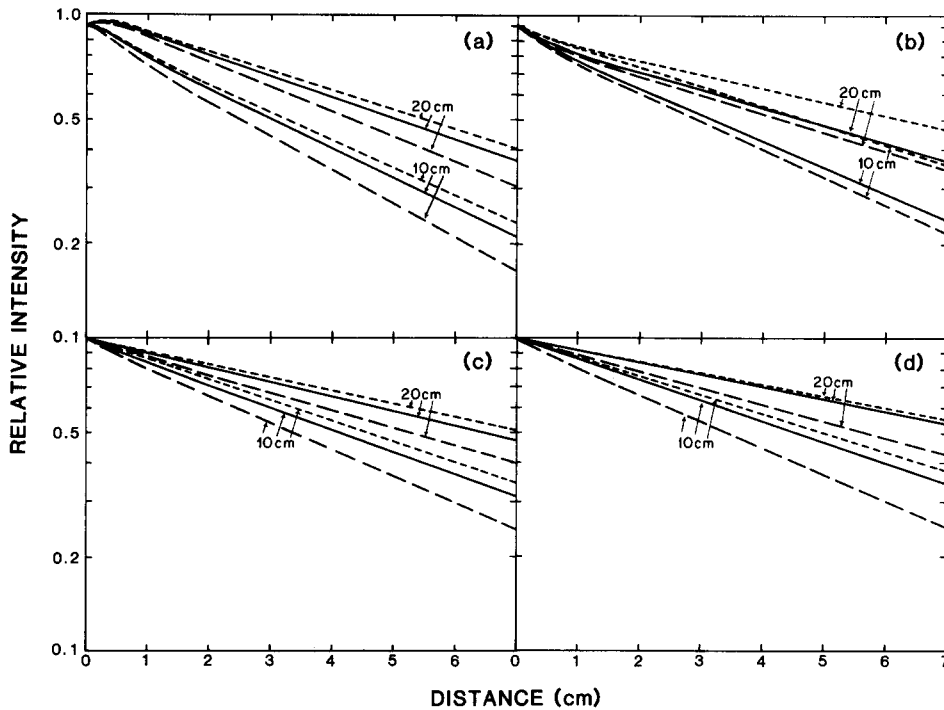
FIG. 14. Line spread functions of scattered radiation recorded on Par Speed (short-dashed curve), Lanex Regular (solid curve), and total-absorption (long-dashed curve) systems, for water phantoms of thicknesses 10 and 20 cm irradiated with incident x rays of energies (a) 40, (b) 60, (c) 80, and (d) 100 keV. The phantom-to-screen spacing was 2.5 cm.

tion is rotationally symmetric. The location at which a scattered photon intercepts the screens depends on the spacing between the phantom and the screens. We used a spacing of 2.5 cm in the calculations. The one-dimensional spatial distribution, i.e., the line spread function, of scattered radiation was determined in this study. The one-dimensional distribution is obtained by integration of the rotationally symmetric distribution along an arbitrary axis,[12] e.g., the y axis. The spatial elements used for the integration of energy absorption was chosen to be infinitely long strips parallel to the y direction; the width of each strip was 2 mm. The central strip was centered on the y axis. The fractional energy absorption in the screens was determined with the methods discussed in Ref. 16. Further blurring of the absorbed energy distribution due to the oblique incidence of scattered photons on the screens of finite thickness and the light diffusion in the phosphor was neglected because these effects were small compared with the broad distribution of scattered radiation. We obtained the spatial distribution of relative absorbed energy density by normalizing the values at each lateral distance to the value at the central spatial element. The energy deposited by the transmitted primary photons was not included in the spatial distributions.

The line spread functions of scattered radiation recorded in the image plane were determined for the nine recording systems used and for various imaging conditions. The results for three of the recording systems are plotted in Figs. 14(a)–14(d). The distributions become broader for thicker phantoms and higher incident energies. The total-absorption system records the narrowest spatial distribution under all input conditions studied. The relative width of the spatial distributions for the eight screen pairs studied depends on the incident photon energy. In general, the width of the spatial distribution for a given screen system drops when the incident photon energy increases from below to above the K edge of the high-Z element in the screen phosphor. This can

be attributed to the increase in energy absorption in the central spatial element; since the scattered photons emerging at small angles have energies very close to that of the primary photons, the probability that these photons will be absorbed in the screens is much higher than that for the low-energy scattered photons, because the energies of the former exceeded the energy of the K edge. Therefore, above the barium K edge (37.4 keV), Quanta II screens detect the narrowest spatial distribution. When the incident energy increases to values above the gadolinium K edge (50.2 keV), Lanex Regular screens record the narrowest distribution. Below the tungsten K edge (69.5 keV), Par Speed screens register the broadest distribution. The broadest distribution is recorded by X-Omatic Regular screens as the incident energy increases above 70 keV, whereas the distributions for Hi-Plus screens and Lanex Regular screens become comparable.

Another notable characteristic of the line spread functions of scattered radiation is their exponential dependence on the lateral distance from the center. Under all of the imaging conditions studied, a linear least-squares regression applied to the logarithm of the relative absorbed energy density values at lateral distances from 2 to 8 cm results in a well-fitting straight line; the correlation coefficient in each case is greater than 0.98. In addition, the summation of all energy deposited beyond a given lateral distance from the center agrees with that calculated analytically from the fitted exponential tail. Therefore, the tails of the line spread functions of scattered radiation can be represented by exponential curves. The behavior of the distributions near the center, however, depends on the imaging conditions. For high-energy incident x rays and a 2.5-cm phantom-to-screen spacing, the trend of the spatial distribution near the center can be approximated closely by the same exponential curve as that used for the tail. For energies of 40 keV and below, the curves increase to a low maximum before decreasing exponentially. The maximum for the low-energy incident x rays is probably

caused by photons which are coherently scattered at small exit angles.

We have studied the line spread functions of scattered radiation at different phantom-to-screen spacings. When the spacing is increased, the spatial distributions become broader, and the intensity of the radiation at each distance from the center decreases. The peak of the distribution shifts to a larger distance; therefore, a peak appears even at energies higher than 40 keV. This indicates that the higher intensity near the center due to small-angle scattering is included in the central spatial element when the spacing is small, so that it is not apparent in the distributions for small spacing and high incident energy.

The line spread function of scattered radiation can be determined experimentally by edge response measurements, as described in Ref. 12. The rotationally symmetric two-dimensional spatial distribution, or the point spread function, can be derived from the line spread function by the Abel transform,[23] or by the method described by Marchand.[24] For a linear, shift-invariant imaging system such as those considered in this study,[9] the point spread function is the base element from which the spatial distribution of scattered radiation for any finite incident x-ray field can be derived by means of spatial convolution.

D. Transfer function analysis of the effect of scattered radiation on image quality

For the linear, shift-invariant imaging systems considered here, the effect of scattered radiation on image quality can be studied by use of transfer function analysis.[25] For simplicity,

the one-dimensional case will be considered in the following discussion. We redefined the line spread function as the one-dimensional spatial distribution of absorbed energy density in the recording system due to scattering radiation, relative to the integral of absorbed energy in the same recording system due to the transmitted primary radiation, when the spatial distribution of the transmitted primary radiation is a one-dimensional Dirac delta function. We then derived[9] that the modulation transfer function (MTF) of the radiation transfer system in the presence of scattered radiation is given by

$$\mathrm{MTF}(\nu) = \mathrm{OTF}(\nu) = \frac{1 + S(\nu)}{1 + S(0)}, \tag{3}$$

where $S(\nu)$ is the Fourier transform of the line spread function of scattered radiation, $S(\nu)/S(0)$ and 1 can be interpreted as the optical transfer functions (OTF) of the subsystems of scattered radiation and primary radiation, respectively. Since the line spread functions of scattered radiation are very broad distributions, their Fourier transforms decrease rapidly to almost zero at very low spatial frequencies. Thus, at high spatial frequencies, $\mathrm{MTF}(\nu)$ will be practically a constant equal to the fraction $1/[1 + S(0)]$. This fraction can be interpreted as the ratio of energy absorbed in the recording system from the primary radiation to the energy absorbed in the same recording system from both primary and scattered radiation; it will be referred to as the primary fraction.

The MTFs of scattered radiation under the imaging conditions studied were calculated for the nine recording systems.[9,26] In general, the MTF becomes almost constant at spatial frequencies higher than 0.2 cycle/cm. This frequency is very low compared with the spatial frequency content of
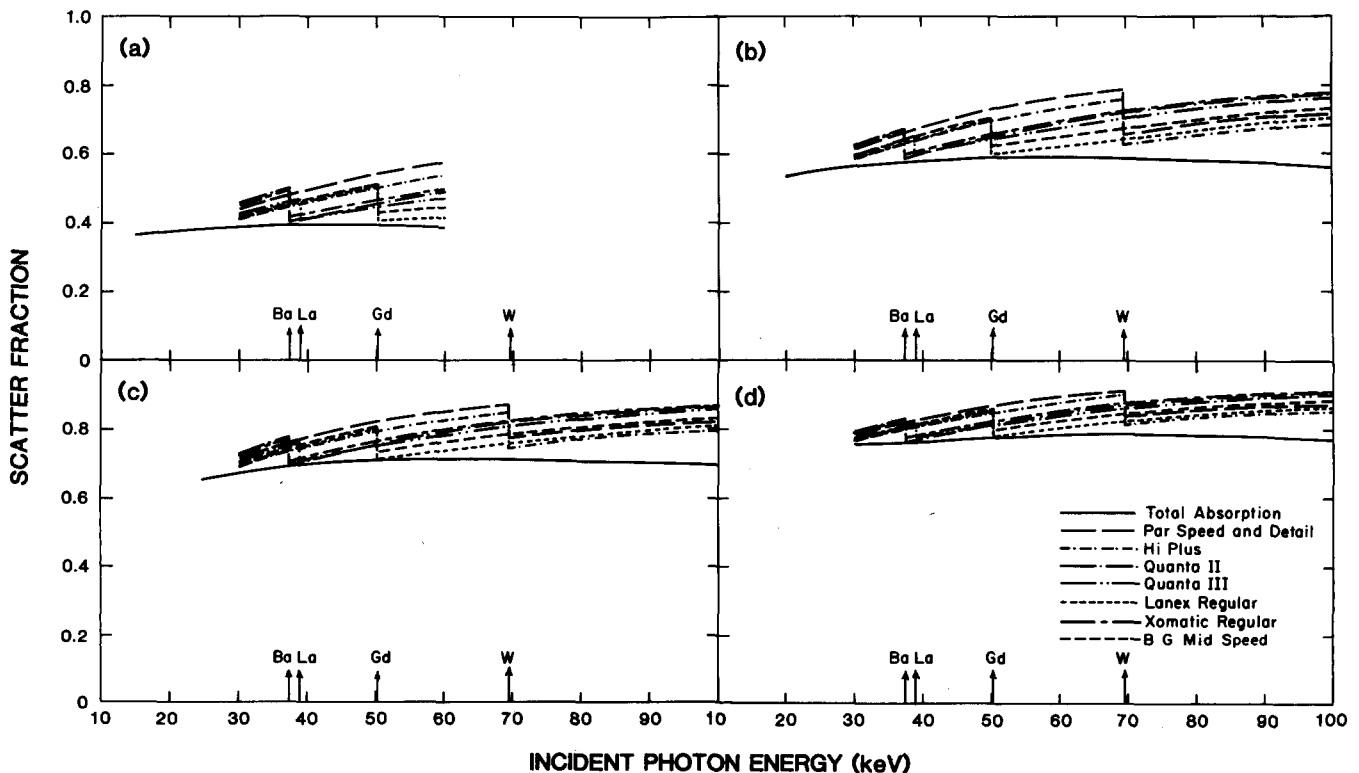

Fig. 15. Dependence of scatter fractions on incident x-ray energy and on the energy response of recording systems, for water phantoms of thicknesses (a) 5, (b) 10, (c) 15, and (d) 20 cm.

the small image details of diagnostic interest and of the MTFs of geometric unsharpness and screen–film unsharpness. Consequently, the effect of scattered radiation on image quality in a radiographic system is a constant reduction of the amplitude of the spatial frequency spectrum, except at very low spatial frequencies. Equivalently, the effect is essentially a reduction of image contrast by a factor equal to the primary fraction, i.e., one minus the scatter fraction. The relative sensitivity of the recording systems to scattered radiation depends upon the energy response of the systems, as will be discussed in the next section. The greater the scatter fraction that a recording system detects, the lower the MTF and therefore the larger the reduction in image contrast.

E. Dependence of scatter fraction on incident energy and recording system

The scatter fraction is defined as the ratio of the energy absorbed in the recording system for the scattered radiation to that from the total (primary plus scattered) radiation. For the linear, shift-invariant imaging system considered here, the total scattered radiation recorded at a point in the image plane for an infinitely broad and uniform primary beam is equivalent to the integral of all recorded scattered radiation for a primary pencil beam of the same intensity. This approach was utilized in the calculation of scatter fractions with the Monte Carlo program.

The scatter fractions recorded by the nine recording systems at various incident photon energies are plotted in Figs. 15(a)–15(d). The scatter fractions recorded by the eight screen pairs for incident energies below 30 keV were not calculated because, as was discussed previously,[16] the assumptions made in the derivation of energy absorption in screens and use of the same sensitometric curve in converting film densities caused by primary radiation and by scattered radiation to absorbed energies may fail in the low-energy range below about 30 keV.

The scatter fraction recorded depends on the energy absorption properties of the recording system. For a total-absorption system, which may be a large NaI crystal or a very thick screen, the scatter fraction is almost independent of the incident photon energy. It also constitutes a lower limit for the scatter fractions detected by the eight screens studied. The larger scatter fraction recorded by screens of finite thickness can be attributed to the higher energy and shorter path length of the primary relative to the scattered photons, resulting in a higher probability for the primary photons than for the scattered photons that they will penetrate the screen phosphor. It should be noted, however, that theoretically the total-absorption system does not always record the minimum scatter fraction nor the narrowest scatter line spread function (Sec. III C) among all recording systems.

The relative sensitivities of the different screens to the scattered radiation depend primarily on their intrinsic properties, such as the phosphor composition and the coating density. In general, for a given system, the scatter fraction increases gradually with increasing incident energy below the K edge of the high-Z element in the phosphor, since the energy of the primary photons increases more rapidly than does the mean energy of the scattered photons (Fig. 12), so

that the increase in the probability of penetrating the screens is more rapid for the primary than for the scattered photons. At the K edge, the cross section of the photoelectric effect increases sharply, resulting in a large absorption probability for primary photons whose energy is just above the K edge. However, the energies of the scattered photons are below the K edge, except for a few coherently scattered photons or small-angle Compton-scattered photons. The relative penetration probability for the scattered photons increases. The scatter fraction therefore drops abruptly across the K edge. The increase in the screen absorption of photons above the K edge is partially offset by the escape of a fraction of the K-fluorescence x rays emitted by the screen phosphor.[16] However, the net increase in the absorption of primary photons remains substantial after the K-escape phenomenon is taken into consideration. As can be seen from Fig. 15, the decrease in the scatter fraction can be more than 10% across the K edge for some phosphor materials and imaging conditions.

It is apparent from Fig. 15 that, depending on the incident energy and the phantom thickness in a radiographic procedure, the scatter fraction can differ by as much as 15% when different screens are used. The strong dependence of the scatter fractions on the energy response of the recording systems indicates that a significant improvement in image contrast may be achieved by proper selection of the recording system for a given imaging technique. The advantage of scatter reduction in this regard could be fully realized if monoenergetic x-ray sources were to become practical for use in medical radiographic procedures, because the energy of the primary and that of the scattered radiation are then clearly distinct. For a polyenergetic incident beam, the transmitted primary spectrum is harder than the scattered spectrum. If a recording system is chosen such that a substantially larger portion of the primary spectrum than of the scattered spectrum is above the K edge of the screen phosphor, the scatter fraction averaged over the spectra can still be reduced, although the improvement may not be as great as for monoenergetic beams. From our previous study of scatter fractions using polyenergetic beams, we found that the Lanex Regular system is least susceptible to the image degradation effect of scattered radiation for diagnostic spectra between 80 and 120 kV.[9,12,26] The improvement in image contrast by use of rare-earth screens with phosphors containing a Gd_2O_2S and La_2O_2S mixture, as compared to the conventional calcium tungstate screens, was observed by Castle[27] under diagnostic imaging conditions.

F. Dependence of scatter-to-primary ratio on field size

For a linear, shift-invariant system, the spatial distribution of scattered radiation, $i_s(x, y)$, recorded by a pair of screens corresponding to a spatial distribution of primary radiation, $i_p(x, y)$, recorded on the same screens is given by a convolution of $i_p(x, y)$ with the appropriate point spread function (PSF) over the field area A:

$$i_s(x, y) = \iint_A i_p(x', y')\text{PSF}(x - x', y - y')dx' \, dy'. \tag{4}$$
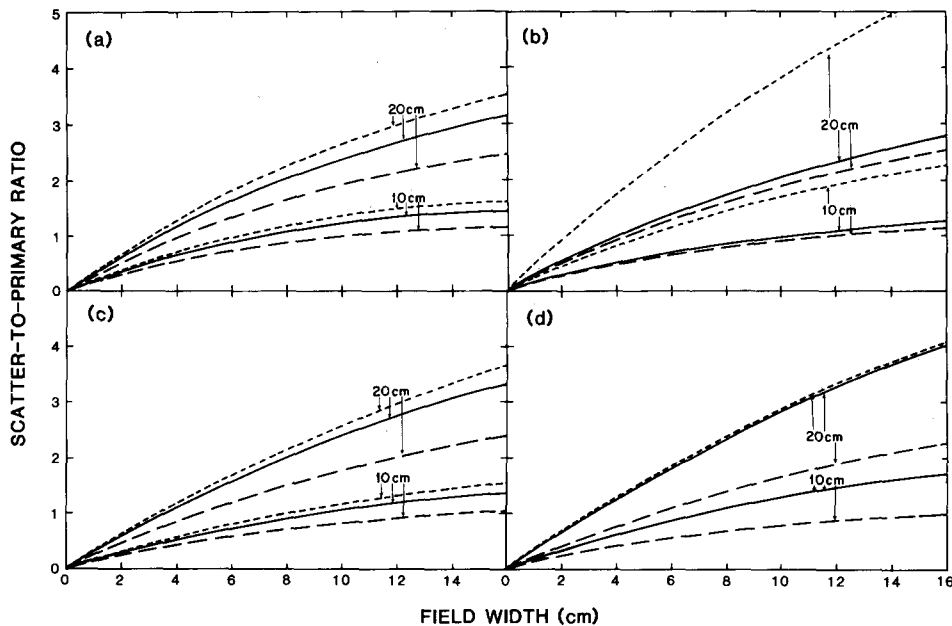
FIG. 16. Dependence of the scatter-to-primary ratio on field width for a phantom-to-screen spacing of 2.5 cm. The scatter-to-primary ratios were recorded by the Par Speed (short-dashed curve), Lanex Regular (solid curve), and total-absorption (long-dashed curve) systems, for water phantoms of thicknesses 10 and 20 cm irradiated with incident x rays of energies (a) 40, (b) 60, (c) 80, and (d) 100 keV.

The situation is simple when the primary radiation is distributed uniformly over A, so that i_p is independent of the coordinates. Equation (4) then becomes

$$i_s(x, y) = i_p \iint_A \text{PSF}(x - x', y - y')dx'\, dy'. \qquad (5)$$

If A is a long slit of width $2w$ and of infinite length parallel to the y axis, the scatter-to-primary (S/P) ratio at the center of a radiation field of width $2w$ is given by

$$\frac{i_s(0)}{i_p} = \int_{-w}^{w} \text{LSF}(x')dx'. \qquad (6)$$

The dependence of the S/P ratio on the field width $2w$ under the various imaging conditions studied was determined from the line spread functions of scattered radiation and is shown in Figs. 16(a)–16(d) for three recording systems. The S/P ratios increase monotonically with increasing field width and asymptotically approach the values for an infinite field.

For a given field width, the S/P ratios recorded by the total-absorption system are the lowest. The relative values of the S/P ratios for the different screens depend on the line spread functions of scattered radiation recorded by the systems. The curves for Par Speed screens and Lanex Regular screens are shown. At 40 keV, the incident energy is below the K edge of the high-Z element in the phosphors of both screens, and the S/P ratios are comparable for the two systems. When the incident energy is increased to 60 keV, which is higher than the energy of the K edge of gadolinium in the Lanex Regular screens, the S/P ratio for these screens decreases considerably for all field widths, resulting in a large difference between the curves for the two systems. When the energy is increased to 80 keV, exceeding the K edge of tungsten in the Par Speed screens, the S/P ratios for these screens also decrease and become similar to the curves for the Lanex Regular system. Finally, at 100 keV, the ratios for the two systems are approximately the same for all field widths, as can be predicted from the similar scatter fractions and line spread functions for the two systems at this energy.

The dependence of the S/P ratios on field width can be determined experimentally with the edge response measurements described previously.[12] Since a monoenergetic source with an output power sufficient for radiographic imaging conditions is not yet available, we employed polyenergetic incident x rays in our measurements. The close agreement between the edge responses determined by Monte Carlo calculations and experimental results which we obtained indicates that the dependence of the S/P ratio on field size for different recording systems can be predicted accurately by means of Monte Carlo methods. The large variation of S/P ratios with field size also confirms the well-known fact that, to minimize image degradation by scattered radiation, the x-ray field in a radiographic procedure must be collimated to a size that is just large enough to cover the area of interest.

IV. DISCUSSION

In this study, we have calculated the physical characteristics of scattered radiation for monoenergetic incident x rays. Since each photon interacts independently with the scattering medium, the corresponding physical characteristics for polyenergetic incident beams can be derived from a weighted sum of the results of their monoenergetic components. The results discussed in this paper can thus be applied to any polyenergetic incident beam. We have determined properties of the scattered radiation for several typical polyenergetic beams from 60 to 100 kV by using the broad spectra as the input to the Monte Carlo program. The dependence of the calculated quantities on the imaging conditions was analyzed in detail elsewhere.[9] The results generally agreed with those which would be expected from the weighted sum of the corresponding properties for monoenergetic x rays.

We assumed a parallel-beam geometry for the incident radiation in our calculations. The resulting shift-invariant property of the imaging system makes it possible to apply spatial convolution for the derivation of many of the physical characteristics of scattered radiation; the photon statistics can thus be improved. The effect of the source-to-phan-

tom distance on the spectral distribution at a depth in the phantom has been discussed in detail in the literature.[4,28] It has been shown that results obtained for a parallel-beam geometry are good approximations to results obtained for a diverging beam geometry, provided that the intensity of the primary radiation and the irradiated area at the depth of interest are kept the same in both cases. In our previous studies,[12,29-31] we found that the scatter fractions and spatial distributions of scattered radiation emerging from a phantom, as measured for a diverging beam at a source-to-film distance (SFD) of 200 cm, and the total transmission of anti-scatter grids (also see discussion below) measured at a SFD of 100 cm agree closely with those calculated for a parallel beam. Therefore, we expect that the physical characteristics of scattered radiation determined in this study will be good approximations to results which will be obtained if a diverging beam geometry is used at long SFDs. Further study will be needed so that the differences in the physical characteristics of scattered radiation between a parallel beam and a diverging beam with a short SFD can be quantified.

The results obtained from Monte Carlo calculations contain statistical uncertainties caused by the probabilistic nature of the method. In this study, all quantities were calculated as the average of ten independent runs, and the statistical uncertainties were estimated as the standard deviation of the mean (SD). The number of incident photons used in each run was varied from 20 000 to 100 000; the lower the incident energy and the thicker the phantom, the larger was the number of incident photons used.

The statistical uncertainty depends on the quantity calculated, the incident energy, as well as the phantom thickness. For quantities such as scatter fraction, mean energy, or mean exit angle, which were derived by integration of all primary or scattered radiation, the SD was about 1%-2%. For the line spread functions of scattered radiation, the SD varied with the distance from the center, since the number of scattered photons decreased with increasing distance. Typically, the SD increased from about 2% near the central ray to about 6% at a lateral distance of 7 cm. For the spectral distributions of scattered radiation, the SD increased from a few percent at the maximum energy to much larger values at the low-energy end of the spectrum. For the angular distributions, the SD was a few percent near the most probable angle and increased toward both the small- and large-angle ranges.

The Monte Carlo results may contain not only these statistical uncertainties, but also systematic errors caused by uncertainties in the physical models of the photon interaction processes and by uncertainties in the input data. For example, we have compared our results of Monte Carlo calculations with published Monte Carlo data. Most published results were calculated with a different irradiation geometry and with neglect of coherent scattering or of the electron-binding effect, except in the work of Reiss and Steinle.[11] These authors did not mention the sources of the incoherent scattering functions and form factors which they used, but they employed the cross-section tables compiled by Storm and Israel in 1967.[32] The photoelectric cross sections of water calculated from these tables are about 5%-11% lower and the coherent-scattering cross sections are about 4%

higher than our cross sections in the energy range from 5 keV (the cutoff energy in our Monte Carlo calculations[12]) to 100 keV. Reiss and Steinle obtained larger numbers of transmitted primary and scattered photons and of backscattered photons, but a smaller number of absorbed photons in water phantoms, than we obtained in our calculations. The differences are within 5% of our results in most cases, but they can be as large as 10%-40% when low-energy photons are incident on a thick phantom, i.e., under conditions where the photoelectric effect and coherent scattering become the dominant interactions, and the statistical uncertainties become very large. Reiss and Steinle also reported a larger total number of scattering processes per 100 photons traced. Their spectral distributions of transmitted scattered photons contained slightly fewer photons in the high-energy region, but more photons in the low-energy region, than those in our spectral distributions (Figs. 10 and 11). The differences observed in the above comparisons are systematic and, in most cases, are greater than the statistical uncertainties. Therefore, they are contributed mainly by differences in the input data used.

In our Monte Carlo calculations, we took into account coherent scattering in water by considering the interference effect of photons coherently scattered by electrons in the same atom; interatomic and intermolecular interference effects were ignored.[12] Recently, some investigators[33,34] suggested that these latter two effects might not be negligible in liquid water; however, they only considered single scattering and did not compare results of photon scattering calculated with and without the latter effects. Muntz et al.[35] observed small-angle scatter components in the exit angle range of 0° to 10° when they measured the spectral and angular distributions of scattered radiation under mammographic imaging conditions (2-6 cm phantom thicknesses, 30-45 kV incident beams); these components were attributed to the intermolecular interference effect of the coherent scattering. Muntz et al. reported small-angle scatter from water, Lucite, and polyethylene, whereas Johns and Yaffe[33] did not observe a small-angle scatter component from Lucite when an 80-kV incident beam was used. Since the importance of these second-order interference effects depends on the incident x-ray energy, the type of scattering material, and also its chemical environment, it is not known at present how they would affect the application of the properties of scattered radiation predicted for water to the estimation of the corresponding properties in soft tissue *in vivo*. We therefore did not incorporate these effects in our Monte Carlo programs.

In our previous study of the performance of antiscatter grids in diagnostic radiology, we used our Monte Carlo programs to simulate photon histories in a water phantom and an antiscatter grid.[11] The transmission of primary radiation and the transmission of total (scattered plus primary) radiation of a grid were calculated. We also measured the radiation transmission of 14 grids (strip densities 33-57 lines/cm, grid ratios 6:1-16:1, lead strip thicknesses 45-50 μ, aluminum interspace) for different thicknesses of water phantoms (15-25 cm thick), x-ray tube potentials (70-120 kV), and screen-film systems (Par Speed/XRP and Lanex Regular/OG).[29-31] A total of 54 transmission values for the var-

ious conditions were measured. We found that the primary and total transmission predicted by the Monte Carlo calculations fell within two standard deviations (SDs of one measurement were about 1.5% and 2.9%, respectively, for the primary transmission and the total transmission) of the experimental values, except at three points. This close agreement indicates that, in the studies of the performance of antiscatter grids under diagnostic imaging conditions, the neglect of second-order interference effects of coherent scattering by liquid water causes an error smaller than the experimental uncertainty. Since a considerable fraction of the large-angle scattered radiation is removed by the antiscatter technique, the effect of small-angle scattered photons such as those arising from coherent scattering should become more noticeable. However, there was no observable systematic deviation of our predictions from the experimental results, as described above.

In addition to investigating grid performance, we have verified the validity of our Monte Carlo calculations by comparing the predictions with experimental measurements in various applications.[12] The good agreement obtained in these studies further indicated that our Monte Carlo calculations can predict the properties of scattered radiation accurately, and that the potential systematic errors do not substantially bias the results.

On the other hand, Muntz et al.[35] calculated by using their radiation transport program in mammography that, when a 4-cm-thick Lucite phantom was irradiated with a 22.1-keV beam, the S/P ratio behind a 15:1 grid varied from about 0.03 to 0.043, depending on the behavior of the angular distribution of scattered radiation at small exit angles (below 5°). In Fig. 2(a), we also showed that the angular distribution of scattered radiation can be dominated by the coherently scattered photons for low-energy x rays incident on thin phantoms.

Therefore, it appears that the influence of the second-order interference effects of coherent scattering on the physical properties of an imaging system varies considerably with the imaging conditions used. The importance of these effects in each case is not well understood. Further work will be needed in order to quantify the systematic errors introduced into the physical characteristics of scattered radiation under various imaging conditions when these are calculated with a Monte Carlo model which neglects the interatomic and intermolecular interference effects.

[1]H. E. Seemann and H. R. Splettstosser, Radiology 62, 575 (1954).
[2]K. H. Reiss and B. Steinle, Tabellen zur Rontgendiagnostik. Teil II (Siemens Aktiengesellschaft, Erlangen, 1973).
[3]K.-G. Strid, Acta Radiol. Suppl. 351 (1976).
[4]W. R. Bruce and H. E. Johns, Br. J. Radiol. Suppl. 9 (1960).
[5]L. Koblinger and P. Zarand, Phys. Med. Biol. 18, 518 (1973).
[6]M. Rosenstein, F. J. Prevo, R. H. Schneider, J. W. Poston, and G. G. Warner, HEW Publication (FDA) No. 76-8030, 1976.
[7]K. Doi and H.-P. Chan, Radiology 135, 199 (1980).
[8]D. R. Dance, Phys. Med. Biol. 25, 25 (1980).
[9]H.-P. Chan, Ph.D. dissertation (The University of Chicago, Chicago, 1981).
[10]H.-P. Chan and K. Doi, Radiology 139, 195 (1981).
[11]H.-P. Chan and K. Doi, Phys. Med. Biol. 27, 785 (1982).
[12]H.-P. Chan and K. Doi, Phys. Med. Biol. 28, 109 (1983).
[13]H.-P. Chan and K. Doi, Med. Phys. 11, 480 (1984).
[14]W. Kalender, Phys. Med. Biol. 26, 835 (1981).
[15]E. Storm and H. I. Israel, Nucl. Data Tables A7, 565 (1970).
[16]H.-P. Chan and K. Doi, Phys. Med. Biol. 28, 565 (1983).
[17]D. T. Cromer and J. T. Waber, International Tables for X-Ray Crystallography, edited by J. A. Ibers and W. C. Hamilton (Kynoch, Birmingham, England, 1974), Vol. 4, pp. 71–147.
[18]H. P. Hanson, F. Herman, J. D. Lea, and S. Skillman, Acta Crystallogr. 17, 1040 (1964).
[19]D. T. Cromer, J. Chem. Phys. 50, 4857 (1969).
[20]G. White-Grodstein, Natl. Bur. Stand. (U.S.) Circ. 583 (1957).
[21]G. T. Barnes, H. M. Cleare, and I. A. Brezovich, Radiology 120, 691 (1976).
[22]J. A. Sorenson, J. A. Nelson, L. T. Niklason, and S. C. Jacobsen, Radiology 134, 227 (1980).
[23]J. C. Dainty and R. Shaw, Image Science (Academic, New York, 1974), p. 210.
[24]E. W. Marchand, J. Opt. Soc. Am. 54, 915 (1964).
[25]C. E. Metz and K. Doi, Phys. Med. Biol. 24, 1079 (1979).
[26]H.-P. Chan and K. Doi, RadioGraphics 2, 378 (1982).
[27]J. W. Castle, Radiology 122, 805 (1977).
[28]H. E. Johns, W. R. Bruce, and W. B. Reid, Br. J. Radiol. 31, 254 (1958).
[29]H.-P. Chan, Y. Higashida, and K. Doi, Med. Phys. (to be published).
[30]H.-P. Chan, P. H. Frank, K. Doi, N. Iida, and S. Sepahdari, Radiology 149(P), 87 (1983) (Abstract), paper No. 227 presented at the 69th Scientific Assembly and Annual Meeting of the Radiology Society of North America.
[31]H.-P. Chan, K. Doi, and Y. Higashida, Med. Phys. 10, 521 (1983) (Abstract), paper No. E2 presented at the 25th Annual Meeting of the American Association of Physicists in Medicine.
[32]E. Storm and H. I. Israel, LASL Report No. LA-3753, 1967.
[33]P. C. Johns and M. J. Yaffe, Med. Phys. 10, 40 (1983).
[34]L. R. M. Morin and A. Berroir, Phys. Med. Biol. 28, 789 (1983).
[35]E. P. Muntz, T. Fewell, R. Jennings, and H. Bernstein, Med. Phys. 10, 819 (1983).